Research Article

Naaser A. Y. Abduh, Abdullah Al-Kahtani, Abdel-Basit Al-Odayni*

Phyto-mediated synthesis of ZnO nanoparticles and their sunlight-driven photocatalytic degradation of cationic and anionic dyes

https://doi.org/10.1515/chem-2024-0093
received June 4, 2024; accepted September 12, 2024

Abstract: In this study, zinc oxide-based nanocatalysts were biosynthesized using *Ocimum basilicum* (OB) and *Olea africana* (OA) leaf aqueous extracts, termed OB-ZnO and OA-ZnO, as a simple, affordable, and environmentally friendly approach. Their characteristics and efficacy in photodegrading cationic dyes (crystal violet and methylene blue) and anionic dyes (methyl orange and naphthol blue black) were investigated. The catalyst's properties were analyzed using various techniques, including Fourier transform infrared, X-ray diffraction, photoluminescence, thermogravimetric analysis, UV-Vis, transmission electron microscopy, energy-dispersive X-ray spectroscopy, and Brunauer–Emmett–Teller. Analysis revealed pure products having a hexagonal wurtzite structure, crystallite sizes of 15.04 and 21.46 nm, surface areas of 23.65 and 7.97 m^2/g, particle sizes of 35 and 170 nm with spherical (uniform) and oval-like (non-uniform) shapes, and optical bandgaps of 3.15 and 3.05 eV, respectively. Photocatalytic applications under sunlight indicated excellent activity of both catalysts against targeted cationic and anionic dyes. Most notably, even though OA-ZnO has a lower surface area than OB-ZnO, it demonstrated greater efficiency. The variation in effectiveness is explained by the lower bandgap value of OA-ZnO and its ability to reduce electron–hole recombination due to its larger crystal size, which accelerates the degradation process. Additionally, both catalysts exhibited high stability after being used four times.

Keywords: biosynthesis, *Ocimum basilicum* extract, *Olea africana* extract, organic dyes, photodegradation, zinc oxide

1 Introduction

Water pollution caused by humans impacts present-day life and future generations, especially considering the recent increase in these pollutants brought on by waste from various industries [1]. Indeed, dyes are known to be among the worst water pollutants due to their widespread use in various industries, such as clothing, accessories, furniture, and plastics [2]. The textile industry is the major contributor to the contamination of natural water resources by discharging its dye-bearing waste directly into surrounding water bodies [3]. Dyes in wastewater can inhibit various processes, including normal physiological activity and photosynthesis in various aquatic plants and animals [4]. Thus, there was a strong desire among the scientific, environmental, and public health communities to tackle pollution and mitigate its effects. Several physical, chemical, and biological methods have been used to remove these pollutants, such as chlorination, reverse osmosis, adsorption, and electrochemical decomposition [5]. However, most of these methods are expensive, require multiple steps, introduce secondary pollutants, or are tedious [6]. More recently, advanced oxidation processes, such as ozonation, radiolysis, sonolysis, photocatalysis, Fenton chemistry, electrochemical oxidation, and wet air oxidation, have emerged as one of the most suitable strategies for water treatment because they are safer and have fewer limitations [7,8]. Among these, photocatalysis has attracted researchers due to its cost-effectiveness, simplicity, environmental friendliness, and its capability to completely eliminate target pollutants.

Photocatalysis using heterogeneous catalysts is a promising methodology and is highly recommended for treating wastewater to eliminate organic contaminants that cannot be removed by conventional methods due to their high chemical stability and limited biodegradability [9]. There are several metal oxide photocatalysts reported in the literature, such as TiO_2, ZnO, SnO_2, CeO_2, MnO_2, and Fe_2O_3 [10]. In addition, doped and mixed oxides were also synthesized and utilized [11]. For the photolysis process to be successful, a preferred

* **Corresponding author: Abdel-Basit Al-Odayni,** Department of Restorative Dental Sciences, College of Dentistry, King Saud University, Riyadh, 11545, Saudi Arabia, e-mail: aalodayni@ksu.edu.sa
Naaser A. Y. Abduh, Abdullah Al-Kahtani: Department of Chemistry, College of Science, King Saud University, Riyadh, 11451, Saudi Arabia

photocatalyst must be selected based on its efficiency, economic viability, and environmental impact.

ZnO is a direct wide-bandgap semiconductor with a bandgap of 3.37 eV and an exciton binding energy of 60 meV. It has gained a lot of interest as a photocatalyst due to its high electron mobility, non-toxicity, photosensitivity, cost-effectiveness, ease of synthesis, and excellent stability [12]. ZnO NPs contain numerous active sites on their surface, allowing for the formation of numerous radicals [13–15]. This property makes them suitable for purification and disinfection applications. Furthermore, due to their peculiar physical and chemical properties, they have also been extensively used in applications related to the optical, chemical, sensing, and electrotechnology industries. Hence, various physical, chemical, and biological methods have been applied for the production of ZnO NPs of various sizes and shapes [16]. Chemical methods typically involve precipitation, sol–gel technology, solvothermal, hydrothermal, microwave techniques, and others [17]. Physical methods combine arc plasma, thermal evaporation, physical vapor deposition, ultrasonic, and laser ablation [18]. These approaches are quite costly and involve harmful chemicals that endanger humans and the environment [19]. Moreover, the use of harsh conditions, such as extended reaction times, high temperatures, and pressures, as well as the incorporation of catalysts during the preparation process, may lead to impure nanoproducts [20]. On the contrary, the biosynthetic route using plant extracts is a green, harmless, biocompatible, and environmentally sustainable method [21].

Although the specific plant-based extract composition varies based on factors like plant type, growing conditions, part used, and extraction method, aqueous extracts are generally known to be lower in volatile compounds compared to their alcoholic counterparts. *Ocimum basilicum* (OB), commonly known as sweet basil, is a fragrant medicinal plant that is mostly used in traditional medicine [22] and as an ornamental plant. The leaf aqueous extract is rich in polyphenols like flavonoids, rosmarinic acid, luteolin, tannins, terpenoids, and glycosides [23]. *Olea africana* (OA) (Arabic name: zaitoon barri) has been reported to have antimalarial and antibacterial activities [24]. The aqueous extract of OA leaves contains flavonoids, biophenols, glycosides, steroids, and tannins [25]. These phytocompounds can potentially be used as reducing and stabilizing agents for NP production. The synthesis of ZnO NPs using plant extracts has sparked a lot of interest in nanotechnology. Plant parts, such as fruits, seeds, leaves, stems, and roots, have been used to manufacture various NPs due to the diverse phytochemicals present in their extracts, which act as stabilizing and reducing agents [26]. Hence, as the extracted chemicals vary depending on the source and the method of extraction, several NPs of various shapes, sizes, and optical properties can be synthesized [27–29].

To the best of our knowledge, no studies have utilized OA leaf aqueous extract for the bio-based synthesis of ZnO or compared its catalytic activity with that of an OB-induced ZnO nanocatalyst for the photodegradation of organic dye pollutants. In this study, ZnO-based nanocatalysts were biosynthesized using OB and OA aqueous extracts as an affordable and environmentally friendly approach. The synthesized catalysts were characterized for their structural, optical, and morphological properties using various techniques, including Fourier transform infrared (FTIR), X-ray diffraction (XRD), UV-Vis, transmission electron microscopy (TEM), energy-dispersive X-ray spectroscopy (EDX), Brunauer–Emmett–Teller (BET), photoluminescence (PL), and thermogravimetric analysis (TGA). The photocatalytic activity of the synthesized photocatalysts was investigated against both cationic (crystal violet [CV] and methylene blue [MB]) and anionic (methyl orange [MO] and naphthol blue black [NBB]) dyes under sunlight.

2 Materials and methods

2.1 Materials

Leaves of OB and OA were collected from the Asir region, a province in the southern part of the Kingdom of Saudi Arabia. The following chemicals were utilized as supplied: MO from British Drug Houses Ltd (BDH) Chemicals Ltd. (Pool, England, UK); MB (95%), CV (≥90%), zinc nitrate hexahydrate ($Zn(NO_3)_2{\cdot}6H_2O$; 98%), and ammonium hydroxide (NH_4OH; 25% in water) from Sigma-Aldrich (St. Louis, MO, USA); NBB from Riedel-de Haën (Seelze, Germany).

2.2 Preparation of aqueous leaf extract

The fresh leaves of OB and OA were sequentially washed with tap and deionized water and then allowed to dry for 3 weeks in the shade. To extract the water-soluble components, 10 g of the dry leaves were chopped into small pieces and immersed in 100 mL of deionized water. The mixture was then heated with stirring for 30 min at 50°C. After cooling, the aqueous leaf extract was filtered through Grade 4 Whatman filter paper and stored in a refrigerator (4–8°C) for later use [30,31].

2.3 Synthesis of ZnO catalysts

The photocatalysts were synthesized as follows: 5 g (0.017 mol) of $Zn(NO_3)_2{\cdot}6H_2O$ was dissolved in 30 mL of OB- or OA-extract and heated at 75°C with stirring for 2 h. Then, drops of NH_4OH (2 M) were added, and the resulting solution was heated for an additional 3 h. To minimize evaporation, the flask containing the mixture was loosely sealed with a glass sheet. After cooling, the resulting precipitate was filtered, washed thoroughly with a 33% ethanol-aqueous solution, and dried in a closed oven overnight at 80°C. The synthesized materials were calcined at 550°C under atmospheric pressure in an air environment, using a heating rate of 20°C/min for 3 h. After cooling (−20°C/min), the materials were stored in sealed vials for subsequent experiments. Under similar conditions, a reference ZnO catalyst was synthesized using deionized water in place of the plant extract (dw-ZnO) for activity comparison.

2.4 Photocatalytic experiments

The photocatalytic performance of the synthesized OB-ZnO, OA-ZnO, and dw-ZnO catalysts in the degradation of selected cationic (CV and MB) and anionic (MO and NBB) dyes was tested under sunlight (intensity = 835 W/m^2) and atmospheric pressure on clear days in October with an average outdoor temperature of 40°C in Riyadh city, Saudi Arabia (24.7136° N, 46.6753° E). Basically, 10 mg of the obtained catalyst (OB-ZnO, OA-ZnO, and dw-ZnO) was added to 10 mL of the examined dye solution (10 mg/L). Before being exposed to sunlight, the suspension was magnetically stirred for 30 min in the dark to achieve an adsorption–desorption equilibrium. To ensure the effectiveness of the catalyst, a blank sample (without a catalyst) was treated in the same manner as the catalytic reaction system. At given time intervals, the mixture was centrifuged for 5 min at 5,000 rpm, and the clear solution was collected for UV-Vis spectrophotometric absorption analysis. The photodegradation efficiency (DE%) was assessed using equation (1):

$$\mathrm{DE}(\%) = \left(\frac{A_0 - A_t}{A_0}\right)100, \tag{1}$$

where A_0 and A_t are the dye concentrations (mg/L) at initial and at time t of irradiation, respectively.

The reusability of the photocatalysts was tested over the course of four catalysis–recovery–reuse cycles. After each catalytic reaction cycle, the catalyst was recovered through centrifugation, washed three times with an acetone/ethanol mixture, dried overnight at 80°C, and then used for the subsequent cycle.

2.5 Characterization

The synthesized OB-ZnO and OA-ZnO NPs were characterized for their structures, morphologies, optical characteristics, compositions, and thermal stabilities using various techniques. The FTIR spectra were recorded using a KBr method in a Perkin Elmer BX spectrometer (Perkin Elmer, Waltham, MA, USA) from 400 to 4,000 cm^{-1}. The XRD patterns were obtained using a Rigaku XtaLAB mini II benchtop X-ray 110 crystallography machine (The Woodlands, TX, USA) with a Cu Kα radiation (λ = 1.5418 Å), over a 2θ range of 10° to 80°, and a scanning rate of 3°/min. The optical properties were analyzed using a Shimadzu UV-2600 spectrophotometer. The TEM images were captured using a JEM-2100F field emission electron microscope (JEOL Ltd., Tokyo, Japan), operating at an 80 kV acceleration voltage. To achieve this, a drop of diluted nanocatalyst suspension in ethanol was deposited onto a lacey-carbon copper grid, dried, and then scanned. The surface area and pore characteristics were analyzed based on N_2 adsorption–desorption isotherms recorded using a Micromeritics Tristar II 3020 (Micromeritics Instrument Corporation, GA, USA), following BET and BJH (Barrett–Joyner–Halenda) calculation methods. The elemental analysis of the target catalysts was confirmed using EDS (X-ray spectrometry) with an X-MaxN system (Oxford Instruments, Abingdon, UK). Thermal analysis was conducted using a Mettler Toledo TGA/DSC Star system (Columbus, OH, USA), performed in the temperature range of 25–700°C with a heating rate of 10°C/min under N_2 gas.

3 Results and discussion

3.1 Synthesis approach

The properties of the synthesized nanophotocatalysts are primarily influenced by the synthesis protocol employed. Phyto-mediated synthesis of NPs offers a green, cost-effective, and straightforward approach. Consequently, the morphological, physical, and chemical properties of the biosynthesized material can be optimized by varying several factors affecting their final properties, including the reaction medium, conditions, and processing techniques. To evaluate the effect of the medium on the structural properties and catalytic activities of the ZnO nanocatalyst, two aqueous extracts (OB extract [OBE] and OS extract [OAE]) were prepared and utilized for the biosynthesis of ZnO. For comparative purposes, ZnO was also synthesized in an extract-free aqueous medium. During the extraction process [30,31],

fresh leaves were thoroughly washed with water to remove dust and minimize microbial contamination. To achieve complete drying while preserving phytochemical integrity, the cleaned leaves were shade-dried at ambient temperature for 3 weeks. In this case, phytocompound transformation and degradation reported under certain storage conditions [32] can be avoided. The catalysts were prepared by heating 30 mL of 0.56 M Zn^{2+} in OBE, OAE, or deionized water for 2 h. To induce particle formation, the medium was alkalized by adding drops of NH_4OH. Figure 1 illustrates a tentative mechanism for the biosynthesis of ZnO NPs facilitated by plant-based phytocompounds (with condensed tannins [CT] representing these compounds; such phytocompounds can function as mono-, bi-, or multidentate) derived from OB and OA.

The aqueous extracts of OB and OA leaves are rich in polyphenols, flavonoids, terpenoids, and tannins [23,25], which play a vital role in the synthesis of nanosized particles through complexation with metal ions. This intermediate step reduces aggregation and fosters the formation of smaller, nanosized particles. The resulting complexes ($CT_n@Zn(H_2O)_m$/$CT_n@Zn(OH)_m$/$CTn@Zn(OH)_m^{x-}$, where n, m, and x are tentative numbers for simplicity) (Figure 1) may undergo decomplexation in basic media, leading to the precipitation of particles, typically in the form of $M(OH)_n$. This process further facilitates the development of the desired nanostructures. To obtain the ready-to-use ZnO-based photocatalysts, the precipitates were subsequently subjected to calcination under air conditions at 550°C for 3 h. This calcination process ensured the production of pure materials by decomposing the zinc hydroxide and tracing extract-derived organic compounds into small, volatile fragments, such as organic gases, CO_2, and H_2O. The calcination temperature is one prominent influencer on the end properties of the photocatalyst [33]. For instance, Sharma et al. [34] have reported that the energy bandgap decreases with increasing calcination temperature from 400 to 600°C, likely due to an increase in the crystallite size. However, a study by Golsheikh et al. [35] reported better optical properties between 500 and 600°C. Accordingly, the calcination temperature in this work was carried out at 550°C, which was selected by different researchers [36,37].

3.2 Characterization

3.2.1 FTIR spectroscopy

Plant extracts generally contain a large number of phytochemicals, such as polyphenols, flavonoids, antibiotics, glycosides, antioxidants, and organic aggregates, which act as reducing and stabilizing agents in NP preparations [38]. Figure 2 shows the FTIR spectra of OB and OA extracts, as well as the corresponding synthesized OB-ZnO and OA-ZnO photocatalysts. As can be seen, the spectra of plant

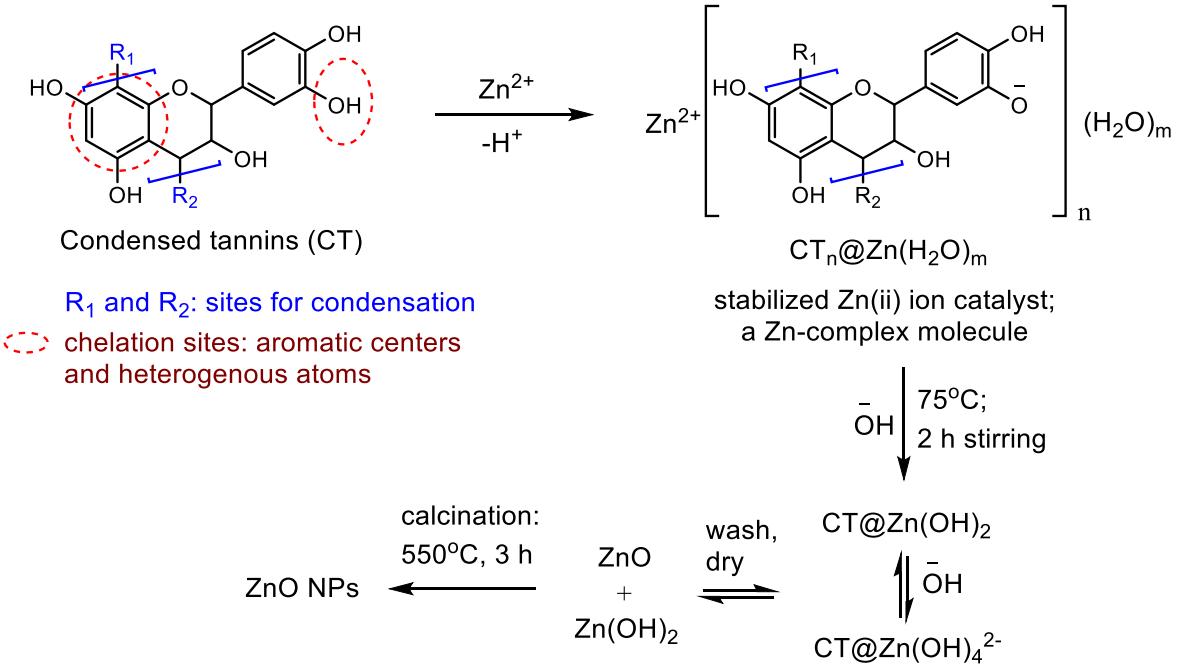

Figure 1: Schematic illustration for the proposed mechanism of biosynthesis of ZnO nanophotocatalysts.

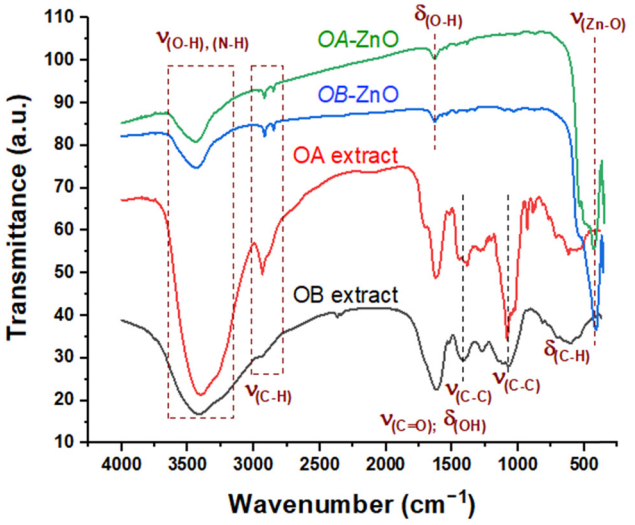

Figure 2: FTIR spectra of OB, OA, OB-ZnO, and OA-ZnO.

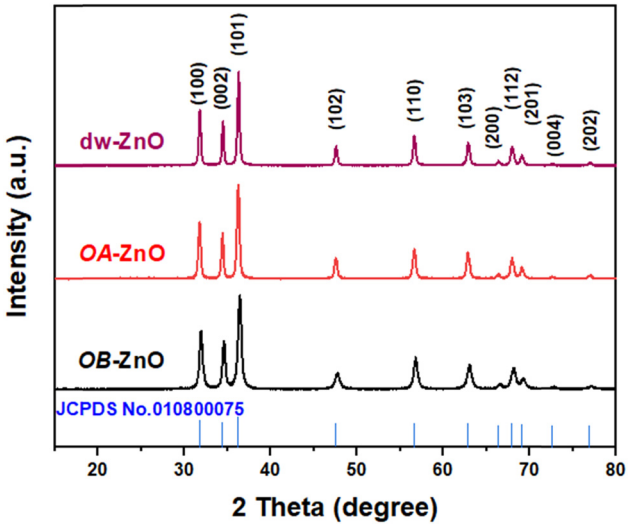

Figure 3: XRD patterns of ZnO (JCPDS No. 0010800075), OB-ZnO, OA-ZnO, and dw-ZnO.

extracts show the presence of different organic functional groups. Hence, the peaks around 3,400 cm^{-1} were assigned to water, O–H, and N–H stretching vibrations, peaks in the range of 3,000–2,770 cm^{-1} to aliphatic C–H bonds, and strong peaks centered at 1,616 cm^{-1} (OB spectrum) and 1,625 cm^{-1} (OA spectrum) correspond to C═O/C═C stretching and N–H bending vibrational modes. According to the literature [39,40], OB leaf aqueous extract contains plenty of bioactive compounds, of which linalool, eugenol, methyl chavicol, and flavonoids are prominent. These compounds are characterized by alcoholic and phenolic OH and C═C bonds. Besides, the peaks for N–H may confirm the presence of amino acids [41]. Additionally, the peaks around 1,416, 1,080, and 600 cm^{-1} were assigned to C–C stretching, C–O stretching, and C–H bending of, e.g., terpenoids like linalool. The spectra of OB–ZnO and OA-ZnO catalysts contain the characteristic peaks of an adequately pure ZnO structure. Hence, the peaks at 3,420 and 1,630 cm^{-1} correspond to Zn–OH and adsorbed water stretching and bending vibrations, respectively. The Zn–O absorption band is clear at 424 and 436 cm^{-1} for OB-ZnO and OA-ZnO [42], respectively; the results are consistent with previous reports [43,44].

3.2.2 XRD analysis

Figure 3 displays the characteristic XRD diffraction peaks of the investigated catalysts, OB-ZnO, OA-ZnO, and dw-ZnO. The patterns exhibit the Bragg diffractions near 31.75°, 34.44°, 36.25°, 47.55°, 56.62°, 62.87°, 66.41°, 67.91°, 69.15°, 72.62°, and 77.03°, corresponding to planes 100, 002, 101, 102, 110, 103, 200, 112, 201, 004, and 202, confirming the hexagonal wurtzite structure of ZnO and matching the conventional data (JCPDS card no. 010800075) and reported results [45,46]. As can be seen, no shifts in the peak positions or new diffractions can be detected, confirming pure structures. Furthermore, the grain size can be calculated using the Scherrer equation, as follows (equation (2)):

$$D = \frac{K\lambda}{\beta\cos\theta}, \tag{2}$$

where D is the average grain size, β is the full width at half-maximum (FWHM), K is a constant, and λ is the wavelength of the incidence X-ray (1.5406 nm).

The crystallite sizes of OB-ZnO, OA-ZnO, and dw-ZnO were found to be 15.04, 21.46, and 25.58 nm, respectively. These findings underscore the potential of the plant extracts to influence the synthesis of smaller ZnO crystallites (OB-ZnO and OA-ZnO) compared to those produced in water (dw-ZnO). As illustrated in Figure 1, the aqueous extracts from the leaves of OB and OA are rich in polyphenols and flavonoids, including tannins, which effectively cap and stabilize metal ions through complex formation. This interaction facilitates the nucleation of crystallites and minimizes aggregation. Furthermore, it is well-established that the specific phytocompounds present in a plant extract can vary depending on the plant species and its part. Although phytocompounds from various plants may share similar functionalities – such as those found in polyphenols and flavonoids – their types and concentrations can differ markedly. This variability contributes to the differences in the sizes of synthesized ZnO nanoparticles [47]. Consequently, the phytocompounds derived from OB appear to inhibit ZnO crystal growth more effectively than those from OA, resulting in the formation of smaller crystallites.

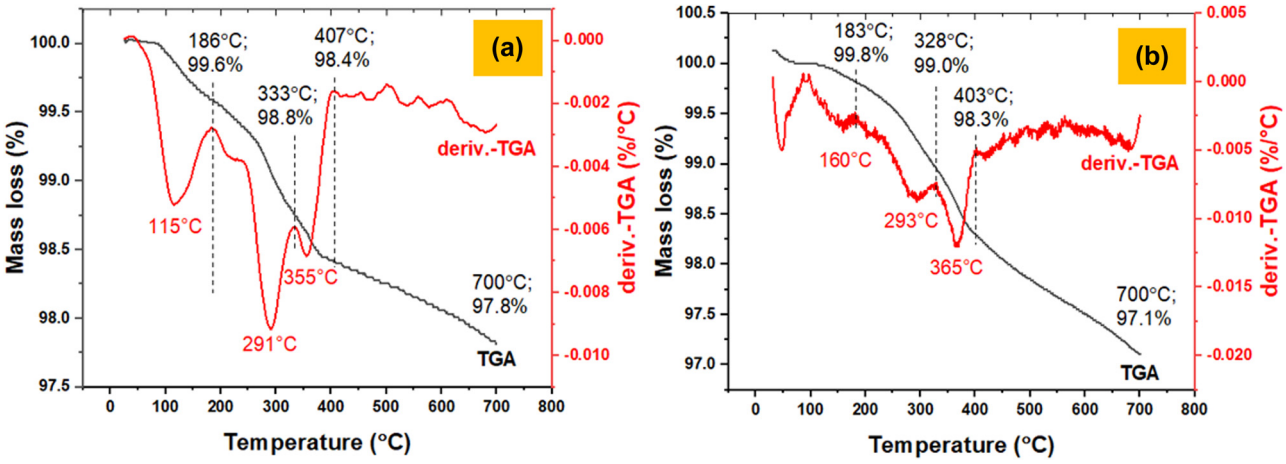

Figure 4: TGA curves of (a) OB-ZnO and (b) OA-ZnO.

3.2.3 TGA

Figure 4 depicts TGA curves for the as-synthesized catalysts, OB-ZnO and OA-ZnO. On the thermograms, three types of water molecules could be detected: adsorption, crystallization, and constitutional water, as further confirmed by FTIR analysis (see Section 3.2.1). The loss of absorbed and crystallized water occurred below 300°C [48,49], observed at derivative-TGA (deriv.-TGA) of 115 and 291°C in the OB–ZnO curve, and 160 and 293°C in the OA–ZnO curve, with a total mass loss of 1.2 and 1.0 wt%, respectively. Above 300°C, the thermograms show peaks for constitutional water – in which the protons attached to the outer oxygens of the polyanions – evaporation [50], i.e., at deriv.-TGA of 355 and 365°C. These results confirm the stability and purity of the as-synthesized catalysts.

3.2.4 Nitrogen adsorption–desorption isotherms

The quantity of adsorbed gas depends on both the adsorption conditions (the relative pressure (P/P^0) and temperature) and the morphology of the solid/gas interface [51]. The adsorption/desorption isotherm can be used to study the surface characteristics. The type of isotherm and desorption hysteresis can offer more information about the material surface, which is valuable for surface area and porosity analysis. The catalyst's morphology typically affects its performance in the photodegradation of organic dyes. Hence, a higher surface area provides more active sites available for organic molecules to adsorb. Furthermore, the higher the number of active sites, the greater the harvested incident light and the better the rate of photodegradation [52]. As shown in Figure 5, OB-ZnO and OA-ZnO

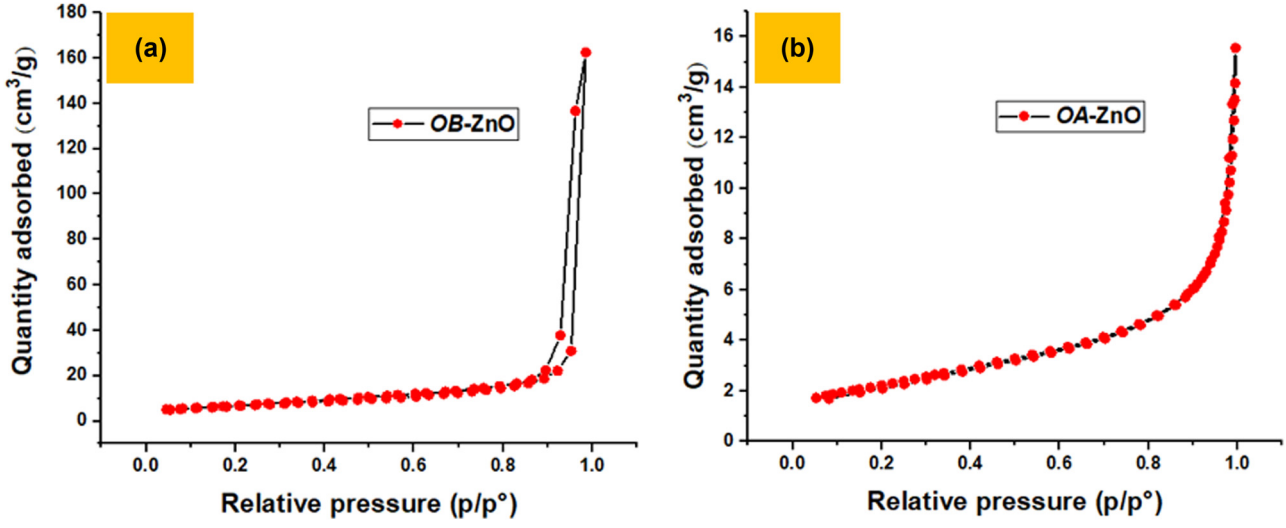

Figure 5: Nitrogen adsorption–desorption isotherms of (a) OB-ZnO and (b) OA-ZnO.

Table 1: BET-surface areas, pore volumes, and pore diameters of OB-ZnO and OA-ZnO

Catalyst	Specific surface area (m^2/g)	Pore volume (cm^3/g)	Pore size (nm)	Crystallite size (XRD; nm)	Particle size (TEM; nm)	Optical bandgap (eV)
OB-ZnO	23.65	0.248	2.75	15.04	35	3.15
OA-ZnO	7.97	0.021	12.06	21.46	170	3.05

catalysts exhibit type IV isotherms. Moreover, the desorption curves indicated type H4 hysteresis loops, as classified by the IUPAC [53]. As can be seen in Table 1, the calculated BET-specific surface area is higher for the OB-ZnO (23.65 m^2/g) than for the OA-ZnO (7.97 m^2/g) NPs; the surface area decreases as crystallite size increases, a result supported by TEM and XRD results.

3.2.5 TEM analysis

Figure 6 shows the TEM micrographs of the biosynthesized OB-ZnO and OA-ZnO catalysts. As can be seen, the OB-ZnO NPs are regular, mostly spherical in shape, while the OA-ZnO particles are more irregular and tend to be longer on one side than the other, resulting in oval- and rod-like shapes. Moreover, the particle size of the OB-ZnO catalyst (average 35 nm) is evidently smaller than that of the OA-ZnO (about 170 nm), which definitely reflects the impact of the extract type on the final properties of the NPs, such as their morphology and, subsequently, their catalytic performance. These results are consistent with the XRD data and demonstrate the ability of the OB extract to inhibit crystal growth more effectively than the OA extract [54]. The particle size determined using XRD is smaller than that measured by an electron microscope (e.g., TEM) due to, on the one hand, the aggregation events observed using the microscope and, on the other hand, reasons related to the Scherer formula, which was originally developed for cubic structures and deviated when applied to other structures [55].

3.2.6 Optical analysis

The electronic structure of the photocatalyst has a substantial impact on its performance [56], which is generally enhanced by reducing the bandgap. Hence, to compute the optical bandgap of the synthesized ZnO NPs, equation (3) was used:

$$(\alpha h\nu)^n = A(h\nu - E_g), \tag{3}$$

where α is the absorption coefficient, h is Planck's constant, ν is the photon frequency, A is a photonic energy-independent constant, $h\nu$ is the photon energy, E_g is the optical bandgap, and n is the semiconductor charge transition (n = 2 or 0.5 for direct and indirect transitions, respectively).

A plot of $(\alpha h\nu)^2$ vs $h\nu$ is displayed in Figure 7, and tangential lines intercepting the abscissa were used to assess the bandgap. Accordingly, the E_g values of OB-ZnO and OA-ZnO were determined to be 3.15 and 3.05 eV, respectively. Such a finding is a classic example of the quantum size effect, where the bandgap energy increases with a decrease in the crystallite size [57]. When particle size decreases, the bandgap widens as electrons and holes are closer together, causing higher kinetic energy due to Coulombic interactions between them [58].

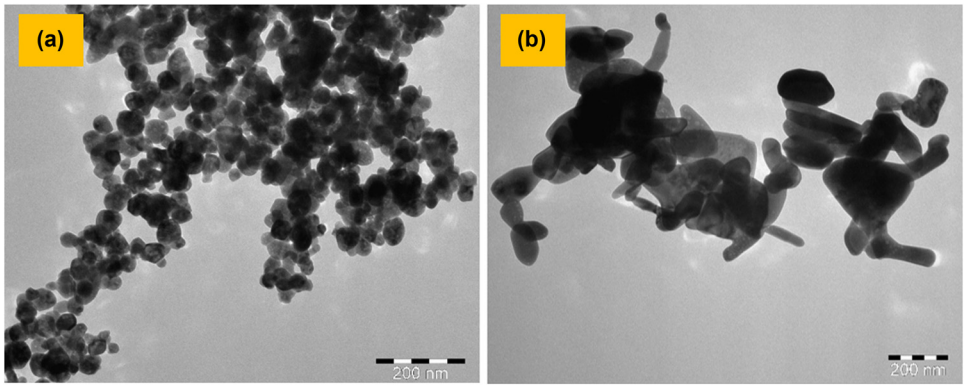

Figure 6: TEM images of (a) OB-ZnO and (b) OA-ZnO.

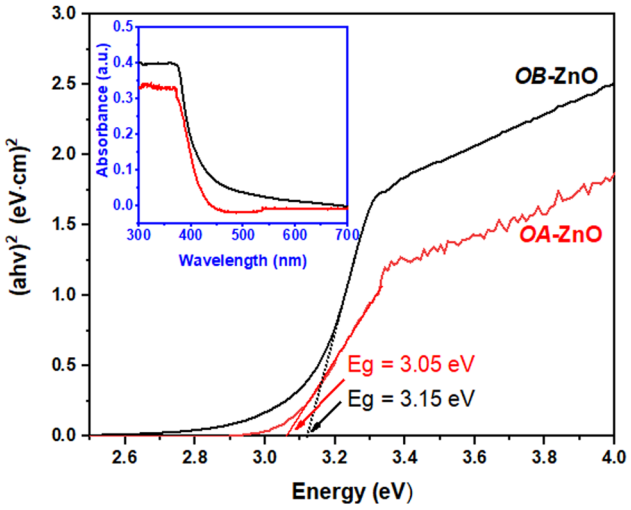

Figure 7: UV-Vis Tauc's plot and (inset) UV-Vis absorption spectra of OB-ZnO and OA-ZnO.

3.2.7 EDS analysis

An EDS test was carried out to determine the elemental composition of the synthesized nanocatalysts, OB-ZnO and OA-ZnO. The EDX spectra, shown in Figure 8, confirm the purity of the produced NPs, as no impurity peaks were detected. Within the accuracy tolerance of the EDS method, the spectra showed a very close Zn-to-O ratio (atomic difference <4.5%) to that theoretically expected, supporting the nominal structures.

3.2.8 PL analysis

PL enables the investigation of the electronic structure and optical properties of semiconductor materials by providing information on surface oxygen vacancies defects, as well as the separation and recombination of photoinduced charge carriers. The intensity of the PL peak is directly related to the rate of electron–hole recombination, i.e., a fast recombination rate results in an intense peak, while a low rate recombination rate (indicating better charge separation) leads to a broader emission peak [59]. The PL spectra shown in Figure 9 demonstrate multi-emission peaks in the range of 350–500 nm. Hence, three emission peaks are more prominent and centered at 406 and 467 nm (blue bands) and 488 nm (green bands). The blue bands in the UV region are assigned to the near band edge, originating from the direct recombination of free excitons through an exciton–exciton collision process [60]. The green band can be attributed to the charge carrier transitions, e.g., between the oxygen vacancy and interstitial oxygen [61,62]. Despite both spectra having a similar emission pattern, the intensity of the emission peaks of OB-ZnO is higher than that of the OA-ZnO nanocatalyst, which is consistent with the literature [63].

3.2.9 Photocatalytic activity of ZnO NPs

The as-synthesized OB-ZnO and OA-ZnO nanocatalysts were evaluated for their photocatalytic activity against cationic dyes (CV, MB) and anionic dyes (MO, NBB) under sunlight irradiation. The photodegradation efficiency of OB-ZnO and OA-ZnO was compared to that of blank (no catalyst) and control (dw-ZnO) samples, as shown in Figure 10. Hence, throughout the degradation period under catalyst-free conditions, a negligible quantity (~3%) of the test dyes was degraded, suggesting the high stability of organic dyes (under experimental conditions). Furthermore, dw-ZnO-catalyzed photodegradation of CV, MB, MO, and NBB was insufficient, reaching only 32, 46, 22 and 28%, respectively. Generally, the efficiency of dye degradation under sunlight increases with the contact time. However, the photocatalytic activity of OA-ZnO is higher than that of OB-ZnO, reflecting the influence of the source type of the phytocompounds used for NP production.

Typically, several factors affect the photocatalytic performance of ZnO, such as the crystallite size, bandgap, carrier recombination, surface area, photon absorption, and the concentration of defects [64]. By closely investigating the degradation profiles, it was noticeable that the amount adsorbed in the first 30 min (conducted in the dark) was significantly greater in the case of OB-ZnO compared to OA-ZnO. In addition, the adsorption of cationic dyes (CV and MB) was found to be higher than that of anionic ones (MO and NBB), possibly due to the abundance of negatively charged active sites on the catalyst surface. Moreover, the detected variation is consistent with the BET data, which suggests a higher surface area of OB-ZnO compared to OA-ZnO, consequently providing more opportunities for dye adsorption. Bandgap and PL analysis also revealed favorable optical properties for the OA-ZnO catalyst over the OB-ZnO catalyst. However, it is reported that the position of the conduction band (CB) and valence band (VB) affects the photocatalytic activity more than the surface area [65]. Moreover, the photocatalytic activity is evidently enhanced for larger crystal sizes. The larger the semiconductor crystal surface, the longer the lifetime of the carrier movement and the lesser the electron–hole recombination [66]. Herein, even though the surface area of the OA-ZnO catalyst is smaller, its improved photocatalytic performance depends on its bandgap, recombination

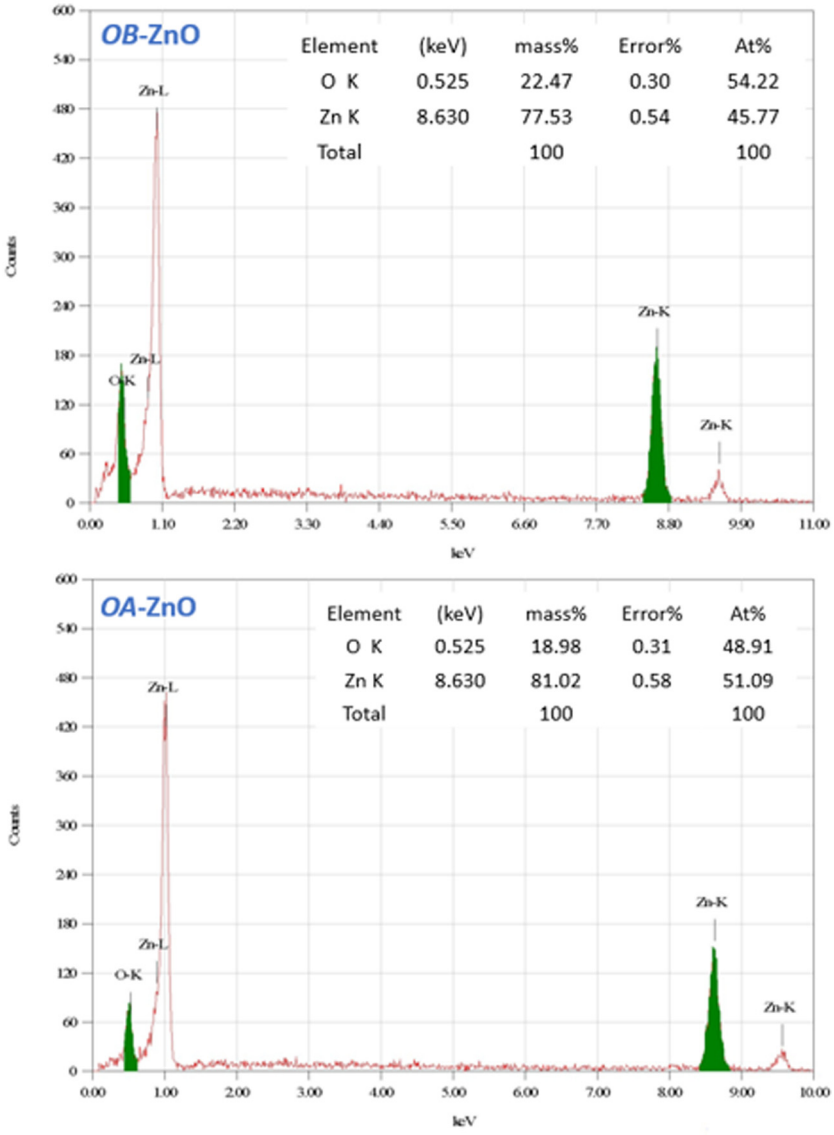

Figure 8: EDS spectra of OB-ZnO and OA-ZnO.

rate, and grain size values, as previously observed [67]. More importantly, the as-synthesized OB-ZnO and OA-ZnO nanocatalysts can be applied for the photodegradation of both cationic and anionic dyes with outstanding efficiency. This demonstrates their utility for colorant removal and water treatment. In general, morphology-controlled ZnO NPs can be obtained by using plant extract-based phytochemicals as reducing and stabilizing agents. Hence, the size, shape, and optical characteristics of ZnO NPs, as well as their photocatalytic activity, are significantly influenced by the source of phytocompounds [68].

As shown in Figure 10, complete photodegradation of the tested dyes in the presence of plant-based ZnO was achieved between 50 and 90 min. The catalytic performance of OA-ZnO is higher than that of OB-ZnO, with nearly 100% degradation efficiency at about 80, 60, 60, and 50 min for OA-ZnO, in contrast to 100, 90, 80, and 60 min for OB-ZnO against CV, MB, MO, and NBB, respectively. Furthermore, the degradation rates of the dyes followed the order of anionic (NBB > MO) > cationic (MB > CV) dyes. Notably, the observed higher degradation rates for the anionic dyes (MO and NBB) relative to their cationic counterparts (CV and MB) can be attributed to their differing acid–base behaviors in solution. Anionic dyes, such as MO and NBB, function as weak acids when dissolved in water [69], releasing H^+ ions and consequently lowering the pH more than the cationic dyes (CV and MB). This reduction in pH negatively impacts the generation of hydroxyl radicals (˙OH), which are crucial

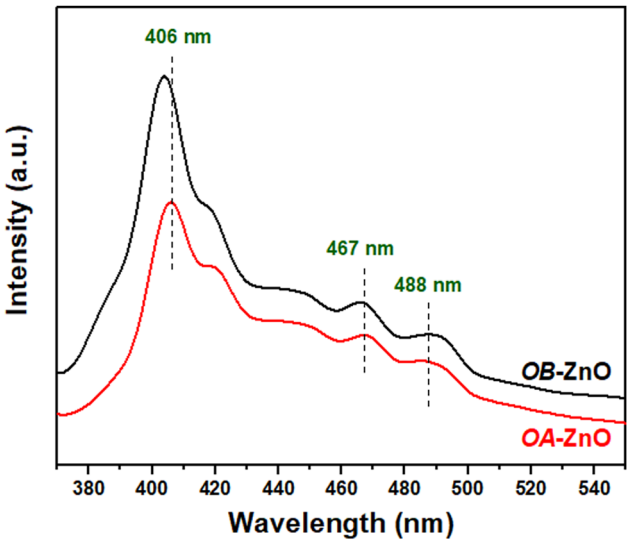

Figure 9: PL spectra of OB-ZnO and OA-ZnO.

for the photodegradation process. Therefore, the lesser photodegradation observed for the cationic dyes compared to the anionic ones may be related to this mechanism [70].

Figure 11 illustrates a proposed photocatalytic degradation mechanism of the investigated organic dyes, CV, MB, MO, and NBB, using ZnO nanophotocatalysts. When ZnO is irradiated with photonic energy equal to or higher than its bandgap, the electrons absorb the light energy and photoexcite from the VB to the CB, thereby generating electron–hole pairs (e^-/h^+). The e^-/h^+ pairs transfer to the ZnO surface and are involved in redox reactions. Basically, the photodegradation depends on the photocatalyst's ability to inhibit recombination of the excitons so that they can transit alternatively to produce reactive oxygen species (ROS). As can be seen, the conduction band electrons (e^-) react with dissolved oxygen species (O_2) to produce superoxide radical ions ($\dot{O}_2^-$) and then hydrogen peroxide

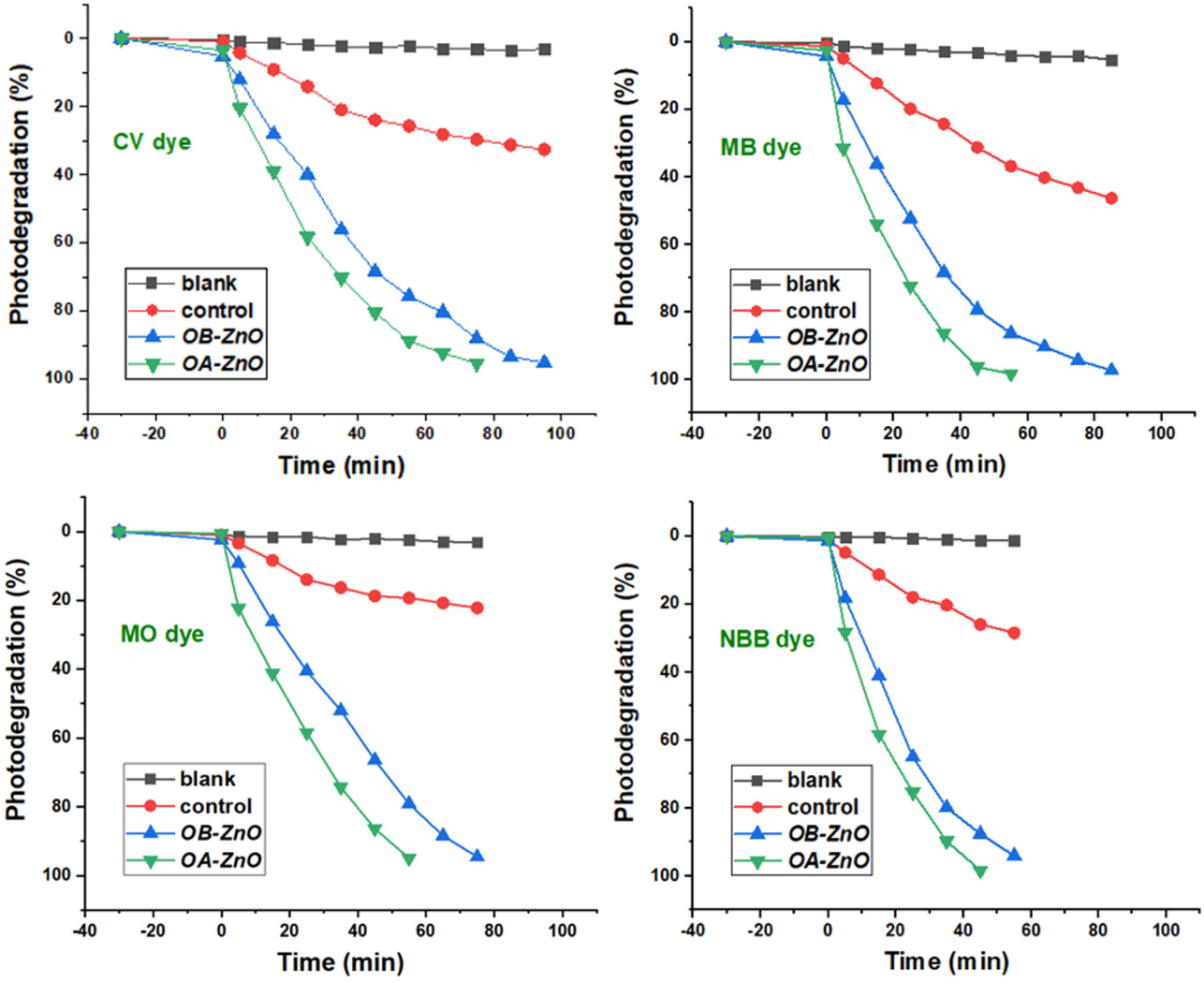

Figure 10: Degradation profile of CV, MB, MO, and NBB under sunlight irradiation in the absence of catalyst (blank) and the presence of OB-ZnO, OA-ZnO, and dw-ZnO photocatalysts.

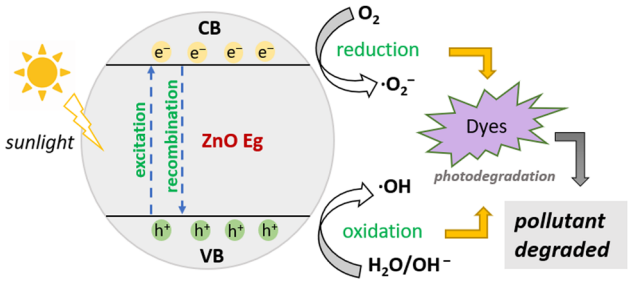

Figure 11: Schematic diagram of the possible mechanism for the photocatalytic degradation of organic dyes on ZnO NPs.

(H_2O_2), which is able to either initiate dye degradation or further react with water (H_2O) to produce hydroxyl radicals ($^{\cdot}OH$). On the other hand, h^+ can react with water or hydroxyl ions (OH^-) to produce hydroxyl radicals. These radicals are critical in the degradation reaction toward water treatment. They react with the adsorbed dyes on the ZnO surface to form intermediate compounds that can degrade to green compounds such as carbon dioxide (CO_2), H_2O, and inorganic compounds [71]. The wide bandgap of ZnO (3.37 eV, corresponding to a wavelength of 368 nm in the UV region), limits its potential use under sunlight irradiation, as only approximately 5% of the solar light can excite ZnO electrons. This low excitation efficiency inadequately inhibits the recombination rate of the generated electron–hole pairs (e^-/h^+). Consequently, enhancing the photocatalytic activity of ZnO requires strategies to broaden its light absorption into the visible region, improve carrier mobility, and increase charge separation. In this study, the observed differences in performance between OB-ZnO and OA-ZnO can be attributed to their distinct properties, which arise from the biosynthesis methods employed, specifically the use of different plant extract sources.

Table 2: Recycling efficiency of OB-ZnO and OA-ZnO in the degradation of CV, MB, MO, and NBB under sunlight irradiation

Catalyst	Dye	Cycle 1	Cycle 2	Cycle 3	Cycle 4	Lost activity (%)
OB-ZnO	CV	95.35	94.04	93.50	91.25	4.20
	MB	98.29	96.35	95.23	92.54	5.85
	MO	94.91	93.58	91.23	90.24	4.92
	NBB	98.30	95.10	94.40	90.89	7.53
OA-ZnO	CV	95.16	94.65	91.87	91.25	4.10
	MB	97.32	94.60	93.69	91.36	6.12
	MO	94.85	92.27	90.58	89.61	5.52
	NBB	94.02	91.82	90.64	88.23	6.15

3.2.10 Reusability

The recovery and reusability of the test catalysts were analyzed for four cycles. The reusability of the catalyst is a crucial factor in evaluating its applicability in real applications; thus, the catalyst's integrity after multiple cycles is essential for its continued use in practical applications. To minimize waste generation and production costs, the catalyst needs to be easily extracted and recycled after the catalytic reaction. Therefore, recycling studies were conducted under similar conditions to the initial photocatalytic experiment. The data acquired from the four cycles are summarized in Table 2, which supports a highly stable catalyst with no significant activity loss for up to four cycles. The decrease in activity after four cycles (lost activity (%), the variance in photodegradation efficiency between the first and fourth cycles) of OB-ZnO nanocatalyst reuse against CV, MB, MO, and NBB was found to be 4.20, 5.85, 4.92, and 7.53%, compared to that of OA-ZnO (4.10, 6.12, 5.52, and 6.15, respectively).

4 Conclusion

In this study, phytochemicals from aqueous extracts of OB and OA plant leaves were used to synthesize ZnO nanocatalysts, known as OB- and OA-ZnO. The obtained ZnO crystals were crystallized in a hexagonal wurtzite structure, exhibiting two distinct morphologies. ZnO induced by OB displayed uniform-sized spherical particles, whereas OA-ZnO resulted in irregular shapes and sizes. The photocatalytic activity of OA-ZnO was higher than that of OB-ZnO NPs against the tested cationic dyes (CV and MB) and anionic dyes (MO and NBB) in a polluted aqueous environment, while all were higher than that of dw-ZnO. It is evident that the surface area was not as critical as the bandgap or recombination rate in determining degradation efficacy. The named catalysts exhibited good stability and activity even after four cycles of reuse. Hence, the method used for synthesis, the feasibility of morphology control, and potential applications in water treatment against certain types of colorants that can be efficiently removed may deserve further studies in the future.

Acknowledgements: The authors thank the Researchers Supporting Project (number RSP2024R266), King Saud University, Riyadh, Saudi Arabia, for their financial support.

Funding information: The research was supported by the Researchers Supporting Project (RSP2024R266), King Saud University, Riyadh, Saudi Arabia.

Author contributions: Conceptualization, Naaser A. Y. Abduh, Abdullah Al-Kahtani, and Abdel-Basit Al-Odayni; formal analysis, Naaser A. Y. Abduh and Abdel-Basit Al-Odayni; investigation, Naaser A. Y. Abduh, Abdullah Al-Kahtani, and Abdel-Basit Al-Odayni; methodology, Naaser A. Y. Abduh, and Abdel-Basit Al-Odayni; writing – original draft, Naaser A. Y. Abduh and Abdel-Basit Al-Odayni; writing – review and editing, Naaser A. Y. Abduh, Abdullah Al-Kahtani, and Abdel-Basit Al-Odayni.

Conflict of interest: The authors declare no conflict of interest.

Data availability statement: The data that support the findings of this study are reported in the manuscript.

References

[1] Kılıç Z. Water pollution: causes, negative effects and prevention methods. Istanb Sabahattin Zaim Üniversitesi Fen Bilimleri Enstitüsü Derg. 2021;3:129–32.

[2] Muthu S. Sustainability in the Textile and Apparel Industries: Sustainable textiles: production, processing, manufacturing & chemistry. Cham (Switzerland): Springer Nature; 2020. ISBN 978–3–030–38545–3 (eBook).

[3] Adane T, Adugna AT, Alemayehu E. Textile industry effluent treatment techniques. J Chem. 2021;2021:1–14.

[4] Al-Tohamy R, Ali SS, Li F, Okasha KM, Mahmoud YA-G, Elsamahy T, et al. A critical review on the treatment of dye-containing wastewater: Ecotoxicological and health concerns of textile dyes and possible remediation approaches for environmental safety. Ecotoxicol Env Saf. 2022;231:113160.

[5] Kaykhaii M, Sasani M, Marghzari S. Removal of dyes from the environment by adsorption process. Chem Mater Eng. 2018;6(2):31–5.

[6] Krishnan S, Rawindran H, Sinnathambi C, Lim J. Comparison of various advanced oxidation processes used in remediation of industrial wastewater laden with recalcitrant pollutants. IOP Conference Series: Materials Science and Engineering. IOP Publishing; 2017.

[7] Deng Y, Zhao R. Advanced oxidation processes (AOPs) in wastewater treatment. Curr Pollut Rep. 2015;1:167–76.

[8] O'Shea KE, Dionysiou DD. Advanced oxidation processes for water treatment. J Phys Chem Lett. 2012;3(15):2112–3.

[9] Aldeen ES, Jalil A, Mim R, Hatta A, Hazril N, Chowdhury A, et al. Environmental remediation of hazardous pollutants using MXene-perovskite-based photocatalysts: A review. Env Res. 2023;234:116576.

[10] Kumari H, Suman S, Ranga R, Chahal S, Devi S, et al. A review on photocatalysis used for wastewater treatment: dye degradation. Water, Air, Soil Pollut. 2023;234(6):349.

[11] Khaki MRD, Shafeeyan MS, Raman AAA, Daud WMAW. Application of doped photocatalysts for organic pollutant degradation-A review. J Env Manag. 2017;198:78–94.

[12] Zhang X, Wang Y, Hou F, Li H, Yang Y, Zhang X, et al. Effects of Ag loading on structural and photocatalytic properties of flower-like ZnO microspheres. Appl Surf Sci. 2017;391:476–83.

[13] Debnath P, Mondal A, Mondal NK. ZnO nanoparticles: a facile synthesized agent for removing dye from aqueous solution in an ecofriendly way. Cognitive Data Models for Sustainable Environment. Cambridge (MA, USA): Academic Press; 2022. p. 163–80

[14] Bopape DA, Motaung DE, Hintsho-Mbita NC. Green synthesis of ZnO: Effect of plant concentration on the morphology, optical properties and photodegradation of dyes and antibiotics in wastewater. Optik. 2022;251:168459.

[15] Udom I, Ram MK, Stefanakos EK, Hepp AF, Goswami DY. One dimensional-ZnO nanostructures: synthesis, properties and environmental applications. Mater Sci Semicond Process. 2013;16(6):2070–83.

[16] Jiang J, Pi J, Cai J. The advancing of zinc oxide nanoparticles for biomedical applications. Bioinorg Chem Appl. 2018;2018:1062562.

[17] Dhoke S. Synthesis of nano-ZnO by chemical method and its characterization. Results Chem. 2023;5:100771.

[18] Jin S-E, Jin H-E. Synthesis, characterization, and three-dimensional structure generation of zinc oxide-based nanomedicine for biomedical applications. Pharmaceutics. 2019;11(11):575.

[19] Singh K, Singh G, Singh J. Sustainable synthesis of biogenic ZnO NPs for mitigation of emerging pollutants and pathogens. Env Res. 2023;219:114952.

[20] Upadhyay P, Jain VK, Sharma S, Shrivastav A, Sharma R. Green and chemically synthesized ZnO nanoparticles: A comparative study. IOP Conference Series: Materials Science and Engineering;. IOP Publishing; 2020.

[21] Naser SS, Ghosh B, Simnani FZ, Singh D, Choudhury A, Nandi A, et al. Emerging trends in the application of green synthesized biocompatible ZnO nanoparticles for translational paradigm in cancer therapy. J Nanotheranostics. 2023;4(3):248–79.

[22] Pedro AC, Moreira F, Granato D, Rosso ND. Extraction of bioactive compounds and free radical scavenging activity of purple basil (Ocimum basilicum L.) leaf extracts as affected by temperature and time. An Acad Bras Cienc. 2016;88(2):1055–68.

[23] Nadeem HR, Akhtar S, Sestili P, Ismail T, Neugart S, Qamar M, et al. Toxicity, antioxidant activity, and phytochemicals of basil (Ocimum basilicum L.) leaves cultivated in Southern Punjab, Pakistan. Foods. 2022;11(9):1239.

[24] Odongo EA, Mutai PC, Amugune BK, Mungai NN. A systematic review of medicinal plants of Kenya used in the management of bacterial infections. Evidence-Based Complementary Altern Med. 2022;2022(1):9089360.

[25] Hashmi MA, Khan A, Hanif M, Farooq U, Perveen S. Traditional uses, phytochemistry, and pharmacology of Olea europaea (olive). Evidence-Based Complementary Altern Med. 2015;2015(1):541591.

[26] Ahmed S, Chaudhry SA, Ikram S. A review on biogenic synthesis of ZnO nanoparticles using plant extracts and microbes: a prospect towards green chemistry. J Photochem Photobiol B: Biol. 2017;166:272–84.

[27] Hamed R, Obeid RZ, Abu-Huwaij R. Plant mediated-green synthesis of zinc oxide nanoparticles: An insight into biomedical applications. Nanotechnol Rev. 2023;12(1):20230112.

[28] Agarwal H, Kumar SV, Rajeshkumar S. A review on green synthesis of zinc oxide nanoparticles–An eco-friendly approach. Resour-Effic Technol. 2017;3(4):406–13.

[29] Hosseingholian A, Gohari SD, Feirahi F, Moammeri F, Mesbahian G, Moghaddam ZS, et al. Recent advances in green synthesized nanoparticles: from production to application. Mater Today Sustainability. 2023;24:100500.
[30] Al Rahbi AS, Al Mawali AH, Al Rawahi SS, Al Dighishi RK, Al Abri FA, Ahmed A, et al. Green synthesis of zinc oxide nanoparticles from Salvadora persica leaf extract: Characterization and studying methyl orange removal by adsorption. Water Pract Technol. 2024;19(4):1219–31.
[31] Alharthi FA, Alghamdi AA, Alothman AA, Almarhoon ZM, Alsulaiman MF, Al-Zaqri N. Green synthesis of ZnO nanostructures using Salvadora Persica leaf extract: applications for photocatalytic degradation of methylene blue dye. Crystals. 2020;10(6):441.
[32] Ioannou I, Hafsa I, Hamdi S, Charbonnel C, Ghoul M. Review of the effects of food processing and formulation on flavonol and anthocyanin behaviour. J Food Eng. 2012;111(2):208–17.
[33] Huang Y, Zheng X, Zhongyi Y, Feng T, Beibei F, Keshan H. Preparation of nitrogen-doped TiO2 nanoparticle catalyst and its catalytic activity under visible light. Chin J Chem Eng. 2007;15(6):802–7.
[34] Sharma V, Sharma J, Kansay V, Sharma VD, Sharma A, Kumar S, et al. The effect of calcination temperatures on the structural and optical properties of zinc oxide nanoparticles and their influence on the photocatalytic degradation of leather dye. Chem Phys Impact. 2023;6:100196.
[35] Golsheikh AM, Kamali KZ, Huang NM, Zak AK. Effect of calcination temperature on performance of ZnO nanoparticles for dye-sensitized solar cells. Powder Technol. 2018;329:282–7.
[36] Akpan UG, Hameed BH. Parameters affecting the photocatalytic degradation of dyes using TiO2-based photocatalysts: a review. J Hazard Mater. 2009;170(2-3):520–9.
[37] El Golli A, Fendrich M, Bazzanella N, Dridi C, Miotello A, Orlandi M. Wastewater remediation with ZnO photocatalysts: green synthesis and solar concentration as an economically and environmentally viable route to application. J Env Manag. 2021;286:112226.
[38] Nguyen NTT, Nguyen LM, Nguyen TTT, Nguyen TT, Nguyen DTC, Tran TV. Formation, antimicrobial activity, and biomedical performance of plant-based nanoparticles: a review. Env Chem Lett. 2022;20(4):2531–71.
[39] Ramana M. Synthesis and characterization of silver nanoparticles from Ocimum basilicum L. var. thyrsiflorum. Eur J Acad Essays. 2014;1(5):5–9.
[40] Aminian AR, Mohebbati R, Boskabady MH. The effect of Ocimum basilicum L. and its main ingredients on respiratory disorders: An experimental, preclinical, and clinical review. Front pharmacology. 2022;12:805391.
[41] Jagadeesh B, Prabha T, Srinivasan K. Improved shelf life of bell capsicum fruits by manipulation of the activities of glycosidases through heat treatment. Indian J Plant Physiol. 2004;9:164–68.
[42] Suwanboon S, Tanattha R, Tanakorn R. Fabrication and properties of nanocrystalline zinc oxide thin film prepared by sol-gel method. J Sci Technol. 2008;30:65–9.
[43] Parthasarathy G, Saroja M, Venkatachalam M, Evanjelene V. Characterization and antibacterial activity of green synthesized ZnO nanoparticles from Ocimum basilicum leaf extract. Adv Biores. 2017;8:29–35.
[44] Alhajri HM, Aloqaili SS, Alterary SS, Alqathama A, Abdalla AN, Alzhrani RM, et al. Olive leaf extracts for a green synthesis of silver-functionalized multi-walled carbon nanotubes. J Funct Biomater. 2022;13(4):224.
[45] Mthana MS, Mthiyane DM, Onwudiwe DC, Singh M. Biosynthesis of ZnO nanoparticles using capsicum Chinense fruit extract and their in vitro cytotoxicity and antioxidant assay. Appl Sci. 2022;12(9):4451.
[46] Mashrai A, Khanam H, Aljawfi RN. Biological synthesis of ZnO nanoparticles using C. albicans and studying their catalytic performance in the synthesis of steroidal pyrazolines. Arab J Chem. 2017;10:S1530–6.
[47] Dallatu Y, Shallangwa G, Africa S. Synthesis and growth of spherical ZnO nanoparticles using different amount of plant extract. J Appl Sci Env Manag. 2020;24(12):2147–51.
[48] Shen Z, Zhou H, Chen H, Xu H, Feng C, Zhou X. Synthesis of nano-zinc oxide loaded on mesoporous silica by coordination effect and its photocatalytic degradation property of methyl orange. Nanomaterials. 2018;8(5):317.
[49] Huang L, Zhou C, Zhang Y, Zhang S, Zhang P. DBHP-functionalized ZnO nanoparticles with improved antioxidant properties as lubricant additives. Langmuir. 2019;35(12):4342–52.
[50] Degirmenci L, Oktar N, Dogu G. ETBE synthesis over silicotungstic acid and tungstophosphoric acid catalysts calcined at different temperatures. Fuel Process Technol. 2010;91(7):737–42.
[51] Seifi S, Levacher D, Razakamanantsoa A, Sebaibi N. Microstructure of dry mortars without cement: specific surface area, pore size and volume distribution analysis. Appl Sci. 2023;13(9):5616.
[52] Reza KM, Kurny A, Gulshan F. Parameters affecting the photocatalytic degradation of dyes using TiO 2: a review. Appl Water Sci. 2017;7:1569–78.
[53] Modwi A, Khezami L, Taha KK, Bessadok JA, Mokraoui S. Photodegradation of a mixture of dyes using Barium doped ZnO nanoparticles. J Mater Sci: Mater Electron. 2019;30:14714–25.
[54] Shaba EY, Jacob JO, Tijani JO, Suleiman MAT. A critical review of synthesis parameters affecting the properties of zinc oxide nanoparticle and its application in wastewater treatment. Appl Water Sci. 2021;11:1–41.
[55] Manzoor U, Siddique S, Ahmed R, Noreen Z, Bokhari H, Ahmad I. Antibacterial, structural and optical characterization of mechanochemically prepared ZnO nanoparticles. PLoS One. 2016;11(5):e0154704.
[56] Alharshan GA, Aboraia AM, Uosif MA, Sharaf IM, Shaaban ER, Saad M, et al. Optical Band Gap Tuning, DFT Understandings, and Photocatalysis Performance of ZnO Nanoparticle-Doped Fe Compounds. Materials. 2023;16(7):2676.
[57] Agarwal S, Jangir LK, Rathore KS, Kumar M, Awasthi K. Morphology-dependent structural and optical properties of ZnO nanostructures. Appl Phys A. 2019;125:1–7.
[58] Nandee R, Chowdhury MA, Kowser MA, Nondy SK, Hossain N, Rasadujjaman M, et al. Bandgap formation in graphene doped with BN, TiO2, Al2O3 and ZnO by sintering process. Results Chem. 2023;6:101229.
[59] Prusty D, Mansingh S, Acharya L, Paramanik L, Parida K. Robust direct Z-scheme exciton transfer dynamics by architecting 3D BiOI MF-supported non-stoichiometric Cu 0.75 In 0.25 S NC nanocomposite for co-catalyst-free photocatalytic hydrogen evolution. RSC Adv. 2022;12(3):1265–77.
[60] Umar A, Hahn Y. ZnO nanosheet networks and hexagonal nanodiscs grown on silicon substrate: growth mechanism and structural and optical properties. Nanotechnology. 2006;17(9):2174.
[61] Zhu X, Zhou Q, Xia Y, Wang J, Chen H, Xu Q, et al. Preparation and characterization of Cu-doped TiO 2 nanomaterials with anatase/rutile/brookite triphasic structure and their photocatalytic activity. J Mater Sci: Mater Electron. 2021;32:21511–24.

[62] Al-Mohaimeed AM, Al-Onazi WA, El-Tohamy MF. Multifunctional eco-friendly synthesis of ZnO nanoparticles in biomedical applications. Molecules. 2022;27(2):579.
[63] Wijesinghe U, Thiripuranathar G, Menaa F, Iqbal H, Razzaq A, Almukhlifi H. Green synthesis, structural characterization and photocatalytic applications of ZnO nanoconjugates using Heliotropium indicum. Catalysts. 2021;11(7):831.
[64] Das A, Nikhil S, Nair RG. Influence of surface morphology on photocatalytic performance of zinc oxide: A review. Nano-Struct Nano-Objects. 2019;19:100353.
[65] Nayan MB, Jagadish K, Abhilash MR, Namratha K, Srikantaswamy S. Comparative study on the effects of surface area, conduction band and valence band positions on the photocatalytic activity of ZnO-M x O y heterostructures. J Water Resour Prot. 2019;11(3):357.
[66] Krobthong S, Rungsawang T, Wongrerkdee S. Comparison of ZnO nanoparticles prepared by precipitation and combustion for UV and sunlight-driven photocatalytic degradation of methylene blue. Toxics. 2023;11(3):266.
[67] Ibhadon AO, Fitzpatrick P. Heterogeneous photocatalysis: recent advances and applications. Catalysts. 2013;3(1):189–218.
[68] Duraimurugan J, Kumar GS, Maadeswaran P, Shanavas S, Anbarasan P, Vasudevan V. Structural, optical and photocatlytic properties of zinc oxide nanoparticles obtained by simple plant extract mediated synthesis. J Mater Sci: Mater Electron. 2019;30:1927–35.
[69] Alghamdi AA, Al-Odayni A-B, Saeed WS, Almutairi MS, Alharthi FA, Aouak T, et al. Adsorption of azo dye methyl orange from aqueous solutions using alkali-activated polypyrrole-based graphene oxide. Molecules. 2019;24(20):3685.
[70] Kahsay MH, Tadesse A, RamaDevi D, Belachew N, Basavaiah K. Green synthesis of zinc oxide nanostructures and investigation of their photocatalytic and bactericidal applications. RSC Adv. 2019;9(63):36967–81.
[71] Yaqoob AA, Mohd Noor NHb, Serra A, Mohamad Ibrahim MN. Advances and challenges in developing efficient graphene oxide-based ZnO photocatalysts for dye photo-oxidation. Nanomaterials. 2020;10(5):932.